Journal of Applied Fluid Mechanics, Vol. 18, No. 12, pp. 2913-2926, 2025.
Available online at www.jafmonline.net, ISSN 1735-3572, EISSN 1735-3645.
https://doi.org/10.47176/jafm.18.12.3664

Plasma Plume Expansion into Ambient Air: OpenFOAM Simulation Using rhoCentralFoam, sonicFoam, twoPhaseEulerFoam Solvers

E. T. Semaha† and G. Miloshevsky

Department of Mechanical and Nuclear Engineering, Virginia Commonwealth University, Richmond, Virginia, 23284, USA

†*Corresponding Author Email: semahaet@vcu.edu*

ABSTRACT

The dynamics of laser-produced plasma plume expansion involves complex interactions between the ablated material and ambient air. This study investigates and compares the performance of three OpenFOAM solvers, namely twoPhaseEulerFoam (tPEF), rhoCentralFoam (rCF), and sonicFoam (sF) using an identical initial setup of geometry and parameters. The primary objective of this study is to affirm the applicability and reliability of the tPEF solver in modeling the laser-produced plasmas for multispecies cases. The focus is on the evaluating the tPEF solver's ability to simulate plasma plume dynamics under atmospheric air pressure. Propagation of plasma shockwave, mesh generation, initial and boundary conditions, and hydrodynamics of single- and multi-phase equations are analyzed. Critical flow variables, such as pressure, velocity, temperature, and density, were monitored spatially and temporally to evaluate the solver performance. The simulation results demonstrate that tPEF produces stable and reliable results that align with physical expectations and previously published data. It was found to be particularly effective in capturing the plume's hydrodynamic features, including multi-species behavior and interaction with the ambient environment. The findings affirm applicability of tPEF for modeling laser-induced plasma plumes, especially in capturing complex fluid dynamics and species evolution. This study will provide computational foundations essential for specific engineering applications involving pulsed laser ablation of multi-component materials.

Article History

Received May 11, 2025
Revised July 10, 2025
Accepted July 31, 2025
Available online October 6, 2025

Keywords:

OpenFOAM solvers
Laser pulses
Material ablation
Plasma plume
Shockwaves

1. INTRODUCTION

Laser ablated plasmas have been used for various purposes over an extended period for producing and removing nanoparticles and clusters, material deposition, material sampling, and other applications (Chrisey & Hubler, 1994; Miller & Haglund, 1998; Puretzky et al., 2000). The plasma plume generated by laser ablation undergoes rapid changes in both spatial and temporal dimensions (Kelly, 1990). Its characteristics are heavily influenced by various parameters such as laser fluence, pulse duration, ambient gas pressure, and composition of gases (Chrisey & Hubler, 1994; Amoruso et al., 2004). With the process of laser ablation that is being discussed, the produced plasma undergoes isothermal (temperature of the plasma remains constant) expansion during the laser pulse and subsequently experiences adiabatic expansion after the laser pulse ends (Singh & Narayan, 1990). During the phase of isothermal expansion, initially the laser light interacts with the solid target. As a result, a plasma plume with high density and low temperature is formed (Torrisi et al., 2002). Subsequently, through collisional ionization and excitation, along with the remaining energy from the laser pulse, the plasma undergoes rapid heating and ionization (Fazio et al., 2014). During the regime of adiabatic expansion, the plasma undergoes expansion into the surrounding air environment (Keidar et al., 2004; Kundrapu & Keidar, 2009). The initiation of the plasma plume can exhibit significant variability depending on the characteristics of the laser (Bäuerle & Bäuerle, 2011). It is accepted that the characteristics of the plasma plume are significantly affected by the ablation procedure, which is intrinsically linked to the fluence and wavelength of the laser (Chryssolouris et al., 1990; Shaikh et al., 2007). Additional fundamental factors that influence the dimensions of plasma plumes are also present (Eliceiri & Grigoropoulos, 2021). Some plasma regions may exhibit

NOMENCLATURE

Acronyms		P	pressure
CFD	Computational Fluid Dynamics	i	phase index (continuous or dispersed)
OpenFOAM	Open-Source Field Operation and Manipulation	k	heat conductivity
rCF	rhoCentralFoam	$\vec{q}$	heat flux
sF	sonicFoam	R	gas constant
tPEF	twoPhaseEulerFoam	S_i	energy of the phase
Roman Symbols		T	temperature
a_i	phase fraction	T_i	temperature of the phases
Cp	specific heat capacities	U	velocity
Cv	specific volume	$\vec{U}$	vector of fluid velocity
D	deformation gradient tensor	***Greek Symbols***	
e	internal energy	μ	dynamic viscosity
E_i	total specific energy of the phases	ρ	density
F_{Di}	lift, drag, and virtual mass	γ	specific heat capacities at constant pressure and volume
K	kinetic energy	$\bar{\tau}$	viscous stress tensor

elevated levels of pressure, temperature, and energetic particles, resulting in a conducive setting for the formation of specific crystallographic structures (Saito et al., 2003). When plasma is generated within a vacuum environment, the resulting plasma plume undergoes adiabatic expansion. The expansion of the ablated material can be accurately characterized by employing the Navier-Stokes equations of hydrodynamics. On the other hand, when the medium surrounding the plume is either air, gas or a liquid, the plume produces compression of the surrounding medium, resulting in the generation of shockwaves. The plasma plume is comprised of a combination of atoms and ions originating from both vaporized material and the surrounding gas (Winefordner et al., 2004; Rai et al., 2007; Anabitarte et al., 2012).

Extensive research has been conducted by multiple groups to thoroughly investigate the complete sequence of events involved in nanosecond laser ablation, including plasma formation and subsequent expansion (Kelly, 1990). These investigations have employed a variety of plasma diagnostic tools and have also involved the development of comprehensive computational models to further enhance our understanding of laser-produced plasmas (Singh & Narayan, 1990; Leboeuf et al., 1996; Gusarov et al., 2000; Gusarov & Smurov, 2002; Harilal et al., 2012). The findings of many studies show the shock structures and fields of temperature, pressure, velocity, and density.

In order to evaluate the capability of the twoPhaseEulerFoam (tPEF) solver in modeling the laser ablation of plasma plumes composed of two compressible fluid phases, it is imperative to conduct a reliable analysis with the single-phase rhoCentralFoam (rCF) and sonicFoam (sF) solvers. This assessment aims to ascertain the accuracy of a transient compressible solver tPEF within the Open Source Field Operation and Manipulation (OpenFOAM) framework (Wang et al., 2008; Harilal et al., 2012; Dawood et al., 2015; Finko & Curreli, 2018). Therefore, we conducted verification and validation of the results obtained from tPEF, rCF and sF models. This was done to ensure that the tPEF model is capable of accurately simulating the plasma plume composed of different species of gases. The results obtained from the tPEF model are expected to closely align with those obtained from the rCF and sF models. The assessment of multiple models for addressing complex problems and determining their level of applicability constitutes a distinct field of study. This concerns the difficulties encountered in the modeling of plasma plume expansion, including the complex rotational dynamics and associated shock wave phenomena (Zhigilei et al., 2009). To effectively tackle the difficulties associated with modeling the expansion of plumes containing diverse species, the utilization of a computational simulation model becomes imperative. Consequently, it is imperative to develop a methodological model that enables the assessment of the efficacy of these solvers, which can replicate outcomes akin to those obtained from practical laboratory experiments on the expansion of plasma plumes. The present model will serve as a reference point and can be employed as a criterion for subsequent experiments.

Our study employs identical parameters for the setup of input data for all solvers, aiming to enhance comprehension of the research. The expansion of plasma plume was characterized at the nanosecond scale by analyzing two-dimensional outputs with high temporal and spatial resolution. This study investigates the effects of initial pressure and temperature on the dynamics of the plasma plume in an atmospheric air pressure. Furthermore, we provide a comprehensive analysis of the impact on the dynamics of the plasma plume.

It is important to note that the primary focus of this paper is to affirm the applicability and reliability of specifically the twoPhaseEulerFoam (tPEF) in modeling laser-produced plasmas for special multispecies cases and so, investigate the dynamics of tPEF plasma plume expansion time evolution into background air. We first compare and contrast tPEF solvers pressure, temperature, density and velocity magnitude results to those produced by single-phase rCF and sF solvers for the purpose of ensuring its applicability to multi-species and compounds for specific modeling. It is important to highlight that

previous studies have also conducted similar but not the same evaluations of different solvers like this study (Karvatskii et al., 2015; Lorenzon & Elaskar, 2015).

2. METHODOLOGY

This section provides an explanation of the parameters and methodology used, including the utilization of OpenFOAM solvers that have the capability to model the flow of compressible non-isothermal fluids (density, viscosity, thermal conductivity, and specific heat may change significantly with temperature). The description of solvers, geometry utilized in the CFD cases, as well as the initial and boundary conditions and the governing equations are given.

2.1 OpenFOAM Solvers

To facilitate affirmation of the modeling results, the three solvers were chosen from the OpenFOAM software package (OpenFOAM v2306). OpenFOAM free-source toolkit is written in C++. It is a widely utilized computational tool in both industrial and scientific domains. The OpenFOAM software package comprises many different solvers that exhibit distinct computational characteristics (Issa, 1986; Kurganov & Tadmor, 2000). The three solvers described below are well suitable to model compressible fluids where the fluid experiences a density change.

The tPEF solver is capable of modelling the laser ablation of plasma plumes with two compressible fluid phases (OpenFOAM, v2306). It is designed to handle scenarios where the phases share a common pressure, while possessing distinct properties for all other quantities (density, velocity, viscosity, etc.) (Kunšek et al., 2021). The phase model of interest can be selected at runtime with the additional capability of representing the model plasma plumes and providing insights into atomic processes, interactions, and phase properties. The various forms of momentum, heat, and mass transfer models can be selected and represented in the phase system (Amidu et al., 2020).

The rCF solver is developed for modelling of the compressible non-isothermal fluid flows and specifically designed to handle density-based problems (Harilal et al., 2012; Ayachit, 2015). The solver is based on the central-upwind numerical schemes (this scheme is used to discretize the Navier-Stokes equations for density, momentum, and energy). The main aim of central upwind scheme is to accurately capture shock waves, rarefaction waves and contact discontinuities without relying on full characteristic decomposition which have been widely recognized for their accuracy and stability in various CFD applications (Kraposhin et al., 2015). It is important to mention that rCF, unlike tPEF and sF solvers, utilizes density-based algorithms.

The sF solver represents a computational framework (Harilal et al., 2012; Bai et al., 2015; OpenCFD Ltd, 2021) capable of modelling the transient problems associated with trans-sonic/supersonic, turbulent flow of a compressible gas. It utilizes the Pressure Implicit (PIMPLE) method (Issa, 1986; Kuvshinnikov & Bondarev, 2017). The fundamental concept behind the PIMPLE approach involves the use of two coupled equations to calculate the pressure, in order to correct the pressure field obtained from a discrete model of the equations of momentum and continuity. Given the potential for velocities modified by the initial adjustment to deviate from the continuity equation, an extra corrector is included to calculate velocities and pressures that satisfy the linearized equations of momentum and continuity. It is worthwhile to note that, while using the same boundary condition across our chosen solvers might seem like a way to ensure a fair comparison, it can lead to inaccurate results. This is because each solver is designed to handle specific problems and boundary conditions must be appropriate for the physical models and algorithms employed by each solver.

2.2 Propagation of Plasma Shockwave

In this sub-section, we present a schematic sketch of shockwave propagation into air ambient as shown in Fig. 1. When a laser is directed on a target, a crater is produced. In our specific case, the plasma plume is formed within the crater with a radius of 0.25 mm and it is generated at a depth of approximately 0.1 mm at the center of the crater. The crater is depicted in the drawing (Fig. 1) as having an oval cross-sectional configuration. It also has an arc that connects a point that is situated on the periphery of the laser spot to a point that is located in the center of the crater. It is symmetrically oval in shape, and the profile of the crater is similar to part of an oval shape.

In our numerical experiment, we set the simulation run time to be 2 μs. It is shown in the sketch that the shockwave is moved away from the crater into the ambient air during the simulation and spreads uniformly. The air ambient within which the simulation was performed is considered as a compressible ideal gas. Both the plasma plume and background gas are motionless at time $t = 0$.

The initial background gas temperature T is set to 300 K. In all cases, the initial internal pressure of air is assumed to be constant 0.1 MPa (1 bar). Also, gas phase properties such as surface tension, drag force, virtual mass heat transfer, lift, phase transfer, wall lubrication turbulent dispersion, etc. were taken into consideration in modeling (these properties will be expressed in the governing equations). Velocity U was initially set to 0 m/s. At time $t = 2$ μs the initial plasma pressure decreased from about 1 MPa to about 0.1 MPa and temperature also decreased to about 300 K from about 2.5×10^4 K. The distance travelled by the plasma plume is about 3 mm on both x- and y-directions.

2.3 Mesh Generation, Initial And Boundary Conditions

The model parameters are configured within a 2D OpenFOAM blockMesh domain with x and y dimensions of 5 mm each. The y-axis is orthogonal to the target surface. A non-uniform crater measuring 0.25 mm by 0.1 mm is positioned along the x and y axes, respectively.

A tetrahedral structured uniform mesh with a grid resolution of 500 × 500 cells is employed to discretize the domain. The domain is filled with air. The mesh with grid

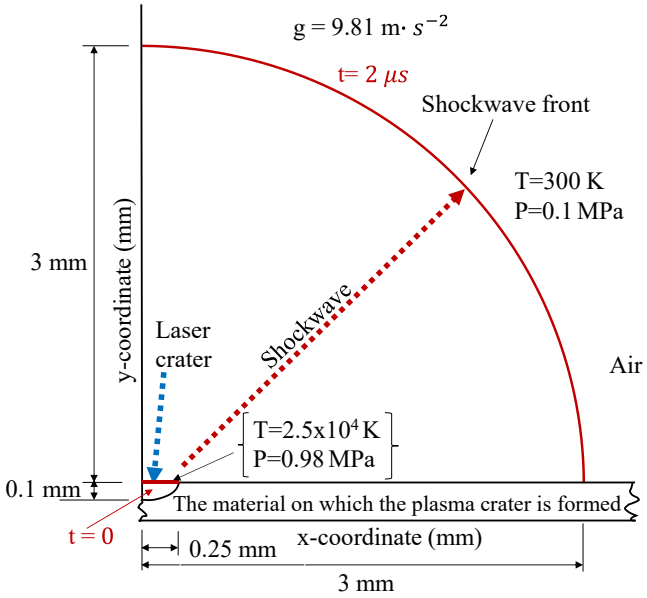

Fig. 1 A schematic sketch illustrating the laser ablation crater and the uniform shockwave propagation into the surrounding air

Table 1 Boundary conditions

Boundary patch types	Pressure (P)	Temperature (T)	Velocity (U)
Left	symmetryPlane	symmetryPlane	symmetryPlane
Right	zeroGradient	zeroGradient	fixedValue
Bottom	zeroGradient	zeroGradient	fixedValue
Top	zeroGradient	zeroGradient	fixedValue
Back	Empty	Empty	Empty
Front	Empty	Empty	Empty
Collapse	Empty	Empty	Empty

sizes of 0.01 mm is applied to the crater along both the x and y axes. The mesh configuration enables the precise resolution of plume dynamics near a laser-induced crater. The list of boundary conditions used in the modelling of plume expansion is presented in Table 1. The "symmetryPlane" condition is employed on the left boundary of the domain to signify that the model displays a characteristic that implies it is mirrored across the boundary, thereby indicating the existence of a symmetry plane, which means, model's geometry is effectively reduced by using a mirrored half.

The boundary conditions for bottom, top, and right boundaries are zero gradient condition for the plasma dynamic quantities, denoted in the table “zeroGradient”. The aforementioned boundary condition enforces a zero gradient condition, whereby the internal field of the domain is extended onto its boundaries. Back, front and collapse boundaries are assigned “Empty” condition, a condition to indicate no calculation or evaluation state condition for cases involving dimensions, specifically 2-D geometries for which our results are presented. The empty condition is also applied to boundaries where the modelling of fluid flow is not needed. The OpenFOAM solvers have a system folder that stores files containing parameters related to the solution process and configuration files. To maintain accuracy, the same Boundary patch types were used for all three OpenFOAM solvers.

The initial ambient conditions of uniform pressure and temperature at 0.1 MPa and 300 K are considered in the simulation, respectively. The specific heat $C_p = 1.005\ \mathrm{kJ/(kg \cdot K)}$ is used. The dynamic air viscosity μ is set to $1.84 \times 10^{-5}\ \mathrm{kg/(m \cdot s)}$ and Prandtl number $\mathrm{Pr} = 0.7$. The value of molar mass $\mathrm{M} = 28.96\ \mathrm{kg/mol}$ is used. The parameters mentioned above are applicable to all three OpenFOAM solvers tPEF, rCF, and sF. Pressure-based tPEF and sF solvers and density-based rCF solver are designed for the modelling of viscous compressible flows, respectively using the conservative formulation. It is important to note that although using identical parameters is an advantageous approach for OpenFOAM solver comparison, there are some limitations to consider. These include the following: (i) differences in solver algorithms to solve specific fluid problems, such as density-based methods, while others use pressure-based PIMPLE algorithms; (ii) numerical sensitivities, which can affect discretization schemes used and can impact the result accuracy and convergence behavior; and (iii) the process can be time-consuming and may require a deep understanding of each solver's specifics in order to produce exact results.

2.4 Governing Equations

The equations implemented in the three OpenFOAM solvers are presented in this Section. Solver tPEF includes two phases as well as the models for their interactions.

Solvers rCF and sF use the same set of the following continuity, momentum and energy equations

$$\frac{\partial \rho}{\partial t} + \nabla \cdot \left(\rho \vec{U}\right) = 0 \tag{1}$$

$$\frac{\partial (\rho U)}{\partial t} + \nabla \cdot (\vec{U}\left(\rho \vec{U}\right)) = -\nabla P - \nabla \cdot \bar{\tau} \tag{2}$$

$$\frac{\partial (\rho E)}{\partial t} + \nabla \cdot \left(\vec{U}(\rho E)\right) = -\nabla \cdot \left(\vec{U} p\right) - \nabla \cdot (\vec{U} \cdot \bar{\tau}) - \nabla \cdot \vec{q} \tag{3}$$

Equation (1) represents the mass conservation equation for continuity in single-phase flows. Equation (2) gives the conservation of momentum neglecting body forces. Equation (3) is depicted as the conservation of total energy. Here ρ represents the mass density, $\vec{U}$ denotes the vector of fluid velocity, $\bar{\tau} = -2\mu\nabla(D)$ is the viscous stress tensor and can be expressed by Newton's Law (Greenshields et al., 2010), where μ is the dynamic viscosity, the deformation gradient tensor $D \equiv \frac{1}{2}\{\nabla\vec{U} + (\nabla\vec{U})^T\}$, and its deviatoric stress component $\nabla(D) \equiv D - \left(\frac{1}{3}\right)\mathrm{tr}(D)I$ with I the unit tensor. P is the pressure, $E = e + U^2/2$ is the total specific energy with e represents the specific internal energy, and $\vec{q} = -k\nabla \mathrm{T}$ represents the heat flux, where T is the temperature and k denotes the heat conductivity. Given the fact that we are considering a plasma plume whose thermal state is determined by the density and pressure, therefore, the equation of state for the perfect gas is $P = \rho RT$ and $e = (\gamma - 1)RT$ is used to close Eqs. (1 - 3). Here, R is the perfect gas constant and the ratio of specific heat capacities at constant pressure and volume is denoted as $\gamma = C_p/C_v$. Note that the above equations implemented in both rCF and sF solvers are all for a single phase.

The numerical solution of the transport of viscous compressible plasma in the ablated plume can be obtained using different numerical solvers (Chen et al., 2014; Finko & Curreli, 2018). The implementation of numerical algorithms is aimed to achieve a precise resolution of shocks and contact discontinuities in compressible subsonic and supersonic flows. Two-phase pressure-based tPEF solver eliminates the need for characteristic decomposition and Jacobian evaluation. This approach offers computational efficiency while utilizing the finite volume method for solving the Navier-Stokes set of equations that govern compressible fluid motion.

The tPEF solver is based on the PIMPLE algorithm to solve the coupled velocity-pressure equations. The equations provided below are applied to a plume consisting of two compressible fluid phases (Greenshields et al., 2010; Freeman et al., 2011; Harilal et al., 2012; Cappelli, 2018; OpenFOAM, 2021). Equation (4) represents the mass conservation of two phases. The index $i = 1,2$ denotes the phase (continuous or dispersed) with the phase fraction α_i. The phase velocity and density are represented by U_i and ρ_i, respectively. Equation (5) describes the momentum conservation, where $(\tau_i + \tau_i^t)$

$$\frac{\partial (\alpha_i \rho_i)}{\partial t} + \nabla \cdot (U_i \alpha_i \rho_i) = 0, \tag{4}$$

$$\frac{\partial (\alpha_i \rho_i U_i)}{\partial t} + \nabla = -\alpha_i \nabla P + \nabla[\alpha_i(\tau_i + \tau_i^t)] + \alpha_i \rho_i g + F_{Di}, \tag{5}$$

$$\frac{\partial (\alpha_i \rho_i E_i)}{\partial t} + \nabla \cdot (\alpha_i \rho_i h_i U_i) + \frac{\partial (\alpha_i \rho_i K)}{\partial t} + \nabla \cdot (\alpha_i \rho_i U_i K) = \frac{\partial (\alpha_i P)}{\partial t} - \nabla[\alpha_i(q_i + q_i^t)] + \nabla \cdot (\alpha_i T_i U_i) + \alpha_i \rho_i U_i g + S_i. \tag{6}$$

provides the combined effects of Reynolds viscous and turbulent stress and the average transfer of momentum at the fluid interface. The fluid pressure is P_i and g states the gravitational constant. The generalized inter-phase momentum drag force term is denoted by F_{Di} (Ishii & Mishima, 1984; Issa, 1986), which guarantees the momentum conservation, especially with multiple phases. Factually, F_{Di} primarily contributes to lift, drag, and virtual mass. The energy equation (6) provides the conservation of total energy of two phases, where the total specific energy of the phases is given by E_i and kinetic energy is indicated by K. Thermal and turbulent convection heat fluxes in the phase are represented by $(q_i + q_i^t)$. The interfacial supply energy of the phase is S_i and T_i symbolizes the temperature of the phases (Gómez-Zarzuela et al., 2021). The set of six equations (4-6) is solved simultaneously for two phases.

It is worth noting that Equation (4) was solved for the phases of fluids and their interactions are incorporated into the solution as implicit corrections in Equations (5) and (6). It is important to point out that the formulated equations are viscous and treat the interfacial supply energy to the phase, species mass diffusion, lift, drag, virtual mass, frictional forces, and viscous stresses. These assumptions are made primarily based on the supersonic characteristics of the later microseconds of plume expansion. During this period, the influence of viscosity becomes apparent as the plume pressure readjusts to atmospheric conditions after the initial expansion caused by the shockwave. Nevertheless, given that the primary focus of this research is on the behavior seen later in the plume development process, an Euler formulation is used to reduce computational complexity. Finally, it is important to note that the sF and tPEF algorithms are pressure based, whereas the rCF (single phase) algorithm is density based (Harilal et al., 2013; Kraposhin et al., 2017; Ghazanfari et al., 2019).

3. RESULTS

3.1 Validation of Shock Front Position in Expanding Plasma Plume Produced by the Fs Laser Pulse

We chose to test the tPEF solver for a position of shock front in an expanding plasma plume against the measured positions using shadowgraphy, Intensified Charge-Coupled Device (ICCD) imaging, and calculated one using CFD simulations that are taken from the previous work (Miloshevsky et al. 2014). As a result, we provide these data gathered for the shock front position and compare them in Fig. 2.

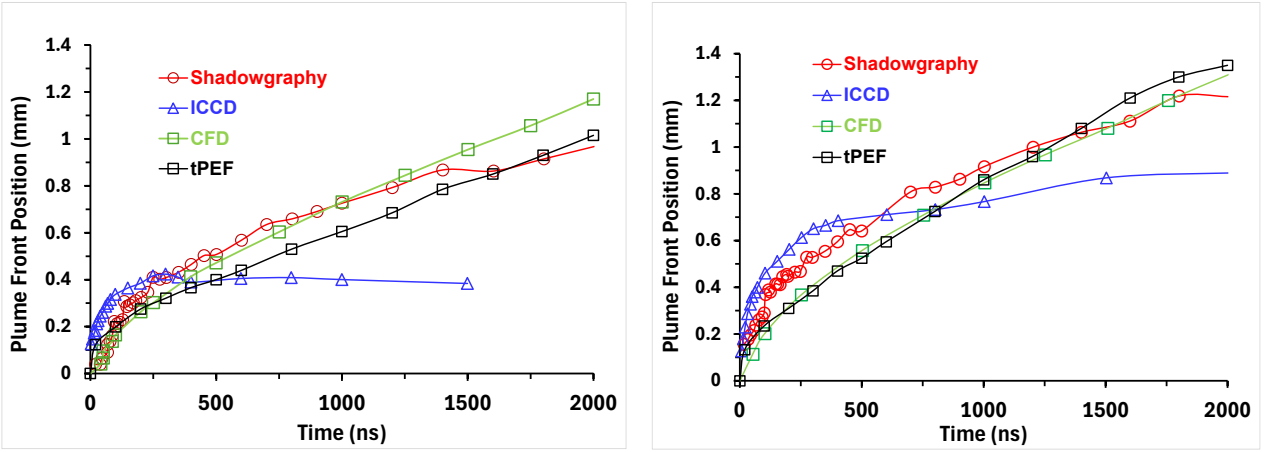

(a) (b)

Fig. 2 The y-coordinate of the shock front in a plasma plume expanding into argon gas calculated using the tPEF solver and compared to experimental data (shadowgraphy, ICCD imaging) and previous CFD result at pressure of (a) 1 atm and (b) 0.5 atm. The profile of shock front obtained from the tPEF solver matches well the experimental and CFD results

The plume shock front predicted by the tPEF solver is seen to be in alignment with previous results at pressure of 1 atmosphere (atm) (0.1 MPa) and 0.5 atm (0.05 MPa). We show the tPEF profile of shock front position in Fig. 2(a) obtained at t = 500 ns (0.5 μs). It can be observed that tPEF predicts a shock position of about 0.4 mm while shadowgraphy shows a position of 0.5 mm with 0.1 mm difference. At 1000 ns (1 μs) tPEF shock front moves 0.6 mm while shadowgraphy and CFD show a position at 0.73 mm, with 0.13 mm difference. It is noticed in Fig. 2(a) that the shock front position calculated from tPEF and CFD computational models are almost similar with shadowgraphy profile located between them.

The expansion of plasma plume is found to slow down at about 375 ns − 400 ns. It is seen that shadowgram is steadily spreading at increasing distances away from the crater. This shows that electron mass mobility is the primary source of emission from the plasma, whereas the plume ambient boundary only produces visible emission from changes in the medium's refraction.

The shock front predicted by ICCD has expanded rapidly during about 300 ns and moved a distance of 0.4 mm. This rapid development could be because of preliminary ambient gas excitation, ionization and rapid illumination of the plasma. The shock front stagnates at about 0.4 mm from 300 ns until 1500 ns. It is an indication of no further increase in plasma gas excitation, hence illumination or most probable inaccurate resolution hampering difficult calibration of the shock front at later moments. Overall, the tPEF solver, shadowgraphy, and CFD findings match well. The shadowgraphy profile shows misalignment at later times, between 1500 and 2000 ns. This could be due to inadequate image quality, making it difficult to measure the position of a shock front.

As illustrated in Fig. 2(b) the position of shock front in argon at 0.5 atm determined by ICCD, shadowgraphy, CFD modeling (previous work), and also calculated using the tPEF solver compare well, especially with the previous CFD computational result until t = 500 ns (Fig. 2(b)). The difference between the curves is smaller than in the case of plume expansion at pressure of 1 atm. It can be observed that the ICCD technique predicts higher position for the shock front from the beginning than the shadowgraphy methodology does comparatively in Fig. 2(a). It can also be observed that the tPEF and CFD computational profiles are behind the shadowgraphy profile before t = 500 ns. The ICCD approach has lower accuracy after t = 500 ns.

Throughout the time evolution of the plume front under consideration, the outcomes of tPEF solver, CFD computational modeling, and shadowgraphy remain in a good alignment. The plasma plume expands very fast at 1 atm and 0.5 atm for the first 300 ns and then starts to slow down. According to the tPEF solver profile in Fig. 2(a) and 2(b), the difference in position of the shock front is only 0.13 mm at $t = 2000$ ns.

3.2 Investigation and Comparison of Performance of tPEF, rCF, and sF Solvers Using an Identical Computational Setup

The profiles of pressure, temperature, density, and velocity of the ablated plume along the centerline (axis taken along the y coordinate) are analyzed. The modeling is carried out on µs timescale and the plasma expansion is studied on millimeter space scale. The profiles exhibit characteristics that are typical of a shock wave propagating away from the target surface into the surrounding atmospheric ambient gas. The pressure profiles are shown in Fig. 3. The modeling was carried out during 2 µs. The highest pressure at the shock wave front predicted by rCF solver has the value of 1.4 MPa. At the same time, tPEF and sF solvers predict the pressure peaks approximately 2 MPa and 0.86 MPa, respectively. Thus, rCF solver demonstrates the highest pressure, while computation from sF solver shows the lowest pressure peak amongst all pressures calculated by the solvers. All three OpenFOAM solvers produce results that are similar.

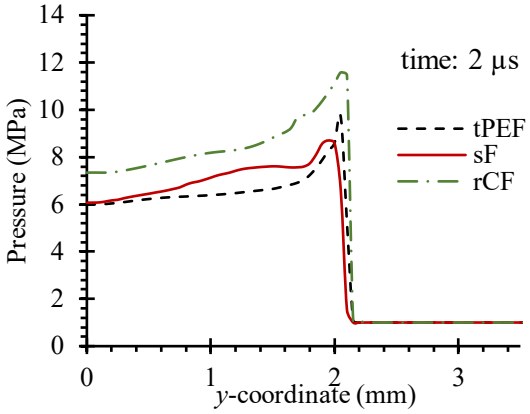

Fig. 3 Comparison of pressure profiles from tPEF, rCF, and sF solvers along the y-coordinate at 2 μs

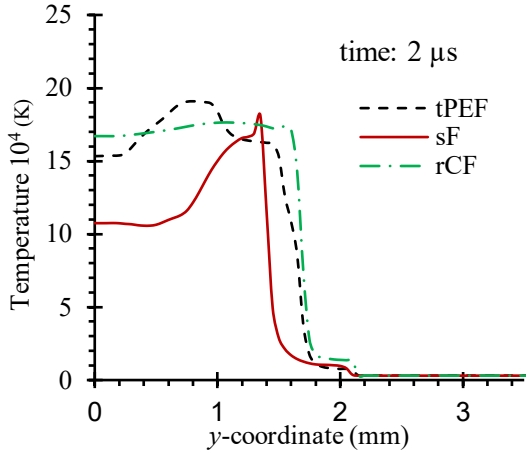

Fig. 4 Comparison of temperature profiles from tPEF, rCF, and sF solvers along the *y*-coordinate at 2 μs

The pressure at the front of shock wave from the rCF solver is wavy as it travels into the ambient, this is an indication of the shock wave that the pressure carries. The pressure of rCF was notably high because of the density-based nature of the solver algorithm, which implies that a denser gas exerts higher pressure than a less gas at a constant temperature. The algorithm considers gases that are more densely packed, resulting in increased collision frequency and greater force per unit area, at a constant temperature, consequently results in increased pressure.

The temperature profiles calculated using tPEF, rCF, and sF solvers are shown in Fig. 4. At time = 2 μs, the highest temperature calculated by tPEF solver is approximately 20,000 K. At the hottest region of the plasma plume, the temperature predicted by rCF and sF solvers are approximately 18,000 K and 14,000 K respectively.

The density profiles obtained from the three solvers are displayed in Fig. 5. Before the start of the simulation, the densities are calculated from the ideal equation of state. At 2 μs, the peak density of sF increases to about 4.4 kg/m³. The peak density calculated from tPEF solver is observed to be about 6.1 kg/m³ and that from rCF is 5.7 kg/m³. At about 2.25 mm and after, the density predicted by all three solvers dropped to 1.6 kg/m³. sF solver recorded the lowest followed by tPEF solver at

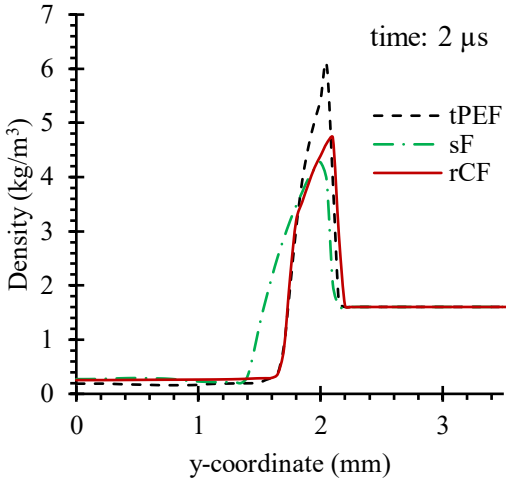

Fig. 5 Comparison of density profiles from tPEF, rCF, and sF solvers along the *y*-coordinate at 2 μs

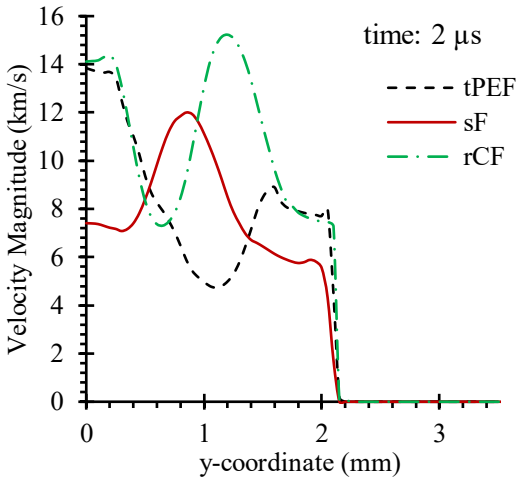

Fig. 6 Comparison of velocity profiles calculated using tPEF, rCF, and sF solvers along the *y*-coordinate at 2 μs

midway, and rCF solver recorded the highest density, as stated earlier, the algorithm of rCF solver is density based. Density and pressure are directly proportional, meaning as density increases, pressure also increases. When a gas is compressed, as in our shock wave front, its density escalates due to the increased pressure of gas inhabiting the volume. Nevertheless, these differences are negligible and do not suggest any significant deviation.

The profiles of velocity magnitude obtained from the three solvers are shown in Fig. 6. Prior to the commencement of the simulation, the velocities are noted to be at rest at time 0. At time = 2 μs, the velocity magnitude of sF reached a peak of approximately 1.3 km/s. The peak velocity calculated by tPEF solver is approximately about 1.4 km/s and rCF solver calculated around 2.2 km/s. At a distance of 2.25 mm on the y-coordinate, the velocities calculated by all three solvers drop to zero, signaling the conclusion of the simulation. The lowest peak was recorded by sF solver, while the computation from rCF solver recorded the highest velocity, followed by calculated velocity from tPEF solver.

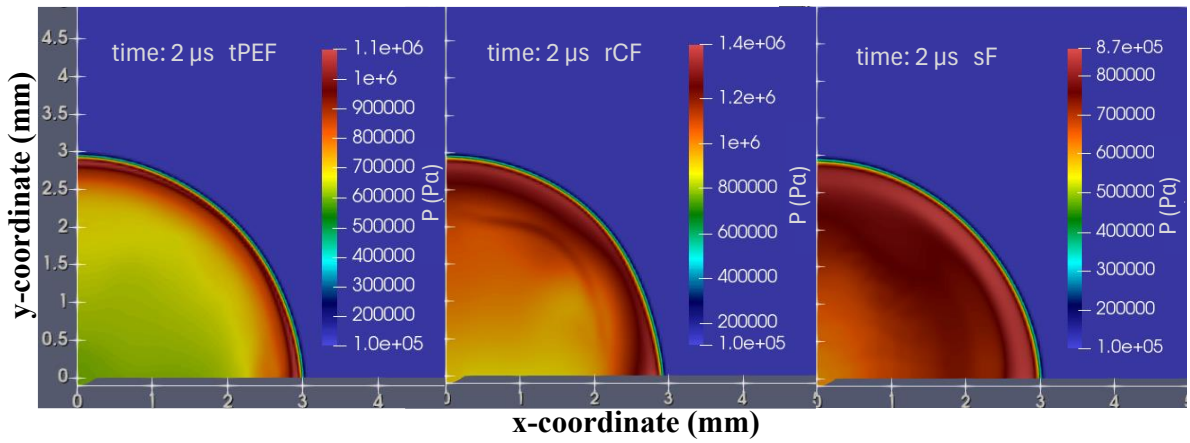

Fig. 7 Color maps of pressure field from tPEF, rCF, and sF solvers for time moment of 2 µs

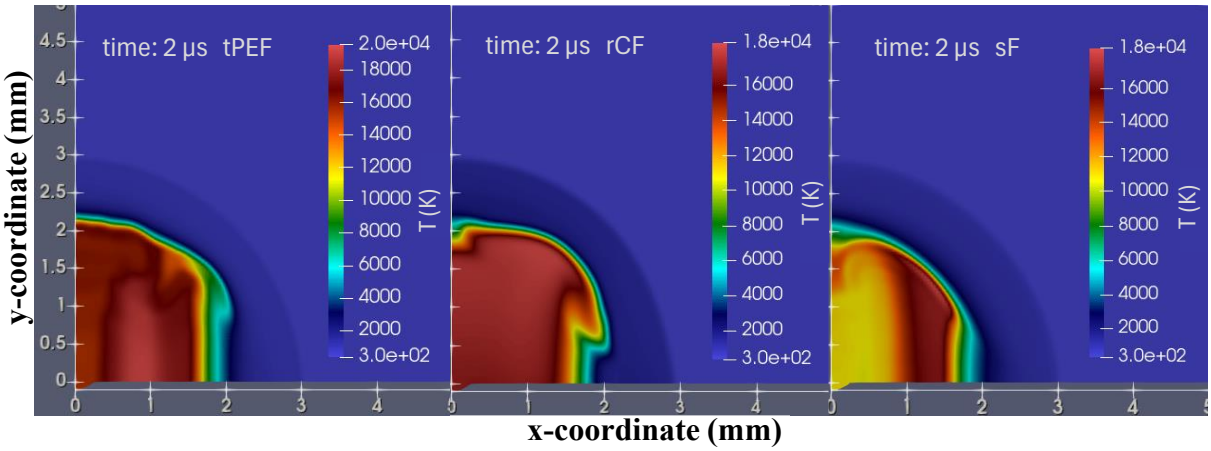

Fig. 8 Color maps of temperature fields from tPEF, rCF, and sF solvers for time moment of 2 µs

However, these minor variations are negligible and do not indicate a significant deviation. As shown in Fig 6, it is evident that rCF consistently maintained the highest velocity throughout the simulation.

The color maps of pressure field calculated using tPEF, rCF, and sF solvers are shown in Fig. 7. It can be seen that plasma expands outward from the target into the surrounding ambient atmosphere. The low-pressure region begins to form at the plume origin and extends outward from the plume's crater (start point). All three solvers predict a sharp rise in the pressure exerted in the normal direction. The lowest pressure at the center region is seen from tPEF solver, but it predicts the mid-highest pressure at the shock front. This is because the shock wave is sucking plasma out of the center to create greater pressure at the shock wave front. The tPEF and rCF solvers predict the highest pressure at shock front, while the pressure calculated from sF solver at shock front is the lowest. An intriguing characteristic can be observed in the plasma core from rCF solver, which consists of a distinct vortex that can be seen to be spreading outward, this is as a result of gas that is more densely packed, resulting in increased collision frequency and greater force per unit area, consequently, results in increased pressure. All tPEF, rCF, and sF maps indicate significant increase in pressure as plasma moves away from the surface of the target. Within the vicinity of the plasma plume, there can be seen to be a great number of oscillating shock waves. The overall evolution of the flow is dominated primarily by rapid transport of the plume front. Although this is difficult to discern from the pressure map.

The temperature color maps showing the plume expansion at 2 µs are illustrated in Fig. 8. In a general sense, the temperature exhibits a high value within the target region of the plume from all three distinct solvers. Also, the main temperature front can be seen to some degree in the maps between 0 and 2 mm on the x-coordinate, and its elevation decreases as the expansion of the plume progresses. The plume exhibits ongoing expansion and subsequently undergoes cooling, resulting in a decrease in temperature as it approaches the leading front. This implies that the temperature of plasma at the shock wave front is relatively low. The high temperature regions shown in all three maps in Fig. 8, form as a result of a decrease in air density behind the main shock front. The higher temperatures in this area also cause the formation of a layer of plasma. There are also temperature variations which are primarily governed by layer of air gas density variation. It should be noted that these higher temperatures are due to slower expansion of the plume close to the wall induces an inward spinning motion of the outer edge of the plume. The phenomenon of "vortex transport" (Finko & Curreli, 2018) describing the organized formation of convective flow structures within

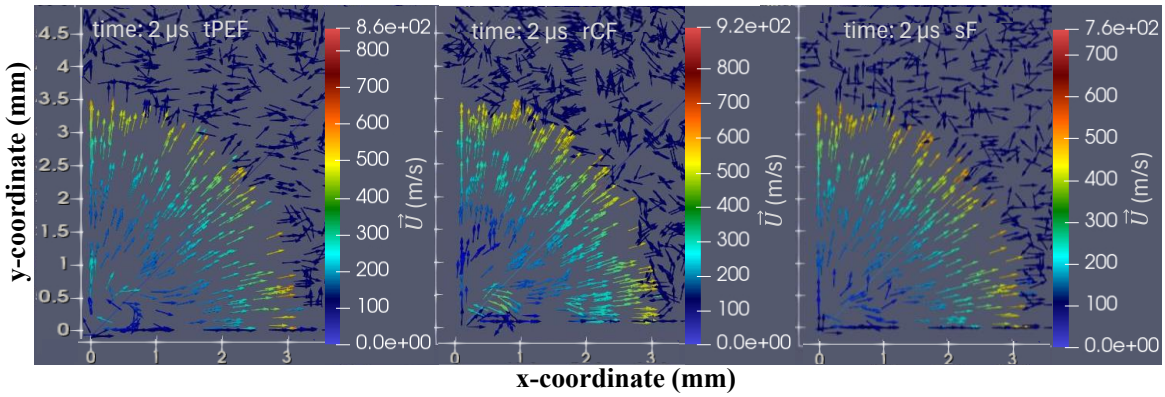

Fig. 9 Maps of vector fields of velocity from tPEF, rCF, and sF solvers for time moment of 2 μs

the plume caused by the fluid expansion past the crater edge geometry significantly increases the thermal energy within the central area of the plume, even during the later stages of plume expansion. In contrast, interactive heating predominantly takes place in the central area of the plume because electrons are ripped away from their atoms forming an ionized gas medium. There is also a faint appearance of the primary shock front, which can be seen in all color maps as the region of slightly elevated temperature that is propagating in front of the plume. This area can be seen from after 2 mm to 3 mm on the x-coordinate in Fig. 8. As the plume continues to expand, it cools even further, reaching temperatures of approximately 300 K at 2 μs, with temperatures even lower near the leading edge.

The maps of velocity vector fields calculated using tPEF, rCF, and sF solvers at 2 μs are shown in Fig. 9. Although there are similarities in the vector field maps, it is important to note that there are also differences among the velocity vector fields produced by the three solvers. The initiation of vortex transport becomes apparent at a distance of 1.5 mm from the origin of cavity, as evidenced by the inward twisting expansion of the plume, which subsequently progresses towards the plume's center. The presence of the vortex is observed to be more pronounced in velocity vector field maps of tPEF and rCF solvers compared to that from sF solver. It is noteworthy that in all three instances of the velocity vector fields, there is a discernible trend of supersonic velocity towards the periphery of the plasma plume.

3.3 Time Evolution of Pressure Field in Plasma Plume Calculated Using Tpef Solver

Since the goal of this paper is to examine the dynamics and time evolution of tPEF plasma plume expansion into background air, this subsection concentrates on specifics of tPEF-predicted plume dynamics. The pressure results obtained from tPEF's solver are analyzed. The time evolution of pressure maps is shown in Fig. 10 at four distinct time moments. The aim is to acquire and provide the details of pressure field at specific times. The color map illustrates the pressure distribution in the surrounding atmosphere ambient. At time 0.1 μs, the plume expands approximately 0.33 mm in the x-direction, however, in the y-direction it expands to 0.25 mm. This occurs due to the fact that the initial size of a plasma plume crater in the y-direction is shallower than that in the x-direction (see Fig. 1). At this same initial time, pressure rises significantly high to about 7.1 MPa. At time 0.4 μs the plume expanded about 1 mm symmetrically in both x-and y-directions at a pressure of 2.8 MPa. At time 1 μs pressure inside the plume drops to 1.6 MPa, though exceeds the ambient atmospheric pressure. Plume also progresses to about 1.8 mm in all directions. Looking at the color maps it can be seen that, pressure continues to be elevated more in the y-direction. Nevertheless, the force in the x-direction also increases and emerges at the center hence the symmetrical shape. At time 2 μs, the plasma plume expanded symmetrically in both the x-and y-coordinate to ≈ 3 mm under a pressure of 1.1 MPa, there is also consistent elevation of pressure at the leading edge of the plume. Uniform pressure establishes across the entire shock front. At the core of the plume, the pressure consistently diminishes compared to the surrounding environment. The decrease in pressure at the center of a plasma plume occurs due to the rapid outward expansion of the plasma from the crater. This expansion results in a reduction in density, which in turn leads to lower pressure at the core of the plume as a consequence of adiabatic expansion principles. Furthermore, based on the principles of gas behavior, when the volume expands while the quantity of particles stays the same, the pressure inevitably diminishes.

3.4 Pressure, Temperature, Density and Velocity Profiles Calculated Using tPEF Solver for Different Times

The profiles of pressure, temperature, mass density, and velocity along the y-component (directed along the target normal) are illustrated in Fig. 11 for various time moments. It is clear that intense shock waves are generated as the plume expands into the surrounding ambient air. As depicted in (Fig. 11(a)), the pressure of the plume rises swiftly within the initial microseconds. The complex movement of plasma plume appears as created shock wave within 0.1 μs and at this time, the pressure within the expanding plume reaches about 5.3 MPa. At time 0.4 μs, plume expands to about 0.64 mm along the y-coordinate and the pressure attains a downward value of 2 MPa. There is also distinct evidence of boundary between the ambient medium and the remaining atmosphere. There are observations of plume transitions into a stage of oscillation

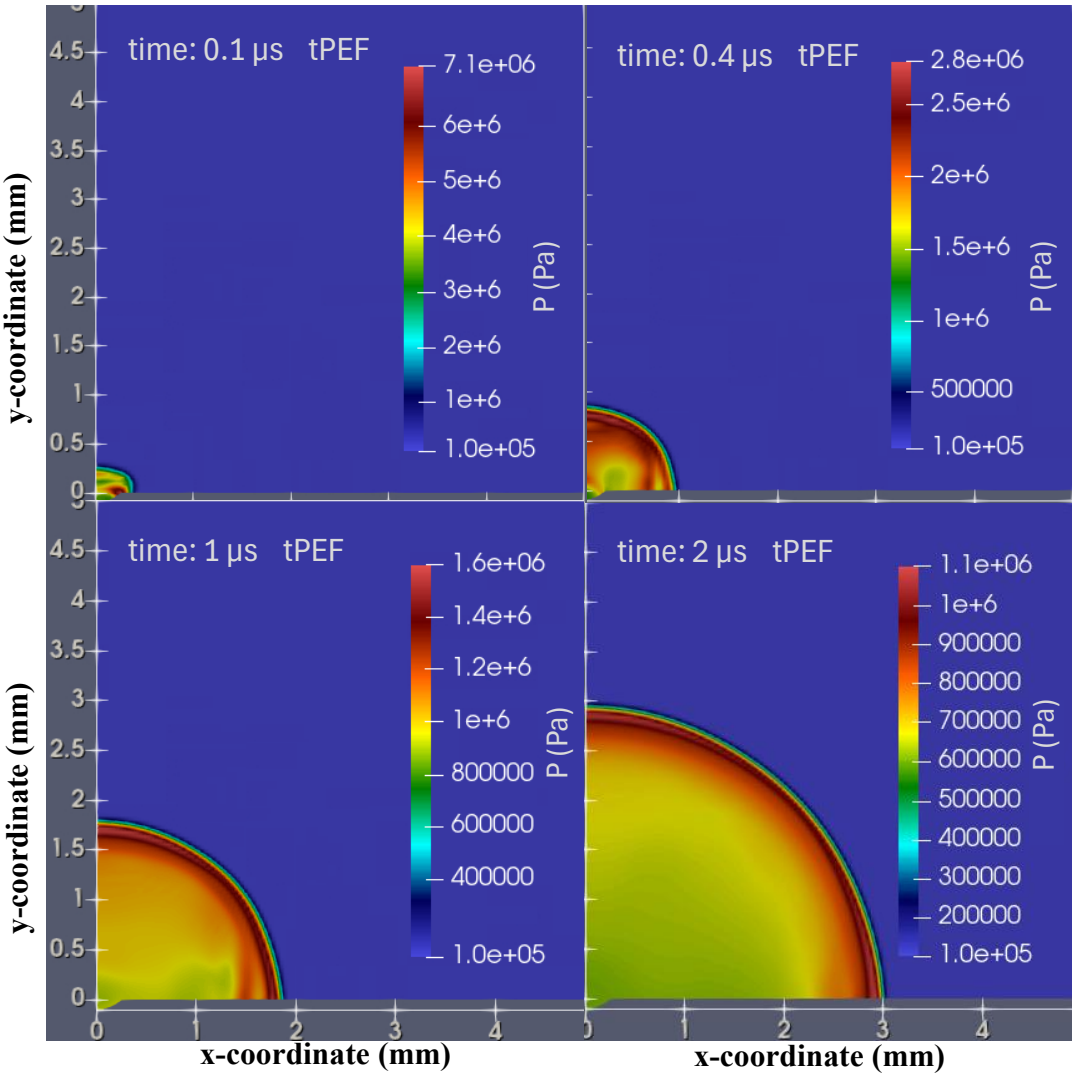

Fig. 10 Color maps of pressure distribution within the generated plume as it expands into background gas at 1 atm for four different times

during its expansion, with not less than 3 shock waves observed in Fig. 11(a). The internal shock waves move multiple times between the center and the front of the plume. These shocks are caused by interactions between the expanding high-pressure plasma and its surrounding gas with lower pressure. Fig. 11(a) aligns with prior experiments (Harilal et al., 2013; Miloshevsky et al., 2014). Figure 11(b) illustrates temperature profiles for different times. At a preliminary moment, the background temperature experiences a significant increase of temperature. At time t = 0.1 μs, the temperature of the plume (Fig. 11(b)) rises rapidly to around 33,500 K from roughly 24,900 K. At time t = 2 μs, the temperature experiences a rapid decline to 300 K at the shock front.

The mass density profile is illustrated in Fig. 11(c), which shows that the mass density increased rapidly to 3.4 kg/m^3 at time t = 0.1 μs. At time 1 μs the plasma density rapidly reached its peak at about 6.5 kg/m^3. At time 2 μs the mass density of the shock front of the plume decreases below the background gas mass density, resulting in the formation of a small shock layer that moves in conjunction with the shock wave. This low-density area left in front is about 0.8 kg/m^3. The mass density of the inner plume is roughly four times less than that of the ambient air background density.

The velocity experiences a rapid increase from 0 to 2.5 km/s (Fig. 11(d)) in a period of 0.1 μs. The velocity value is even higher at shorter durations (not displayed), which aligns with the initial temperatures of the plasma. The speed of the shock wave diminishes considerably at time 0.1 μs. At time greater than 0.4 μs, there appear multiple internal shock waves emerging in and around the center of the plume. They move in the same direction as the primary wave expands and then curls back towards the center of the plume. Following the internal shock the plasma movement is directed back toward the center of the plume. This can be because of higher velocity in the surrounding allowing the expanding plasma to be compressed by the surrounding gas, which results in a high recoil velocity. This high recoil velocity may create backward reflections, which are shock or pressure waves that propagate back toward the target. Due to the creation of a ring-like vortex that pulls denser gases back toward the target, the flow of plasma in the plume near the target's surface is very complicated at this point (also see Fig.10).

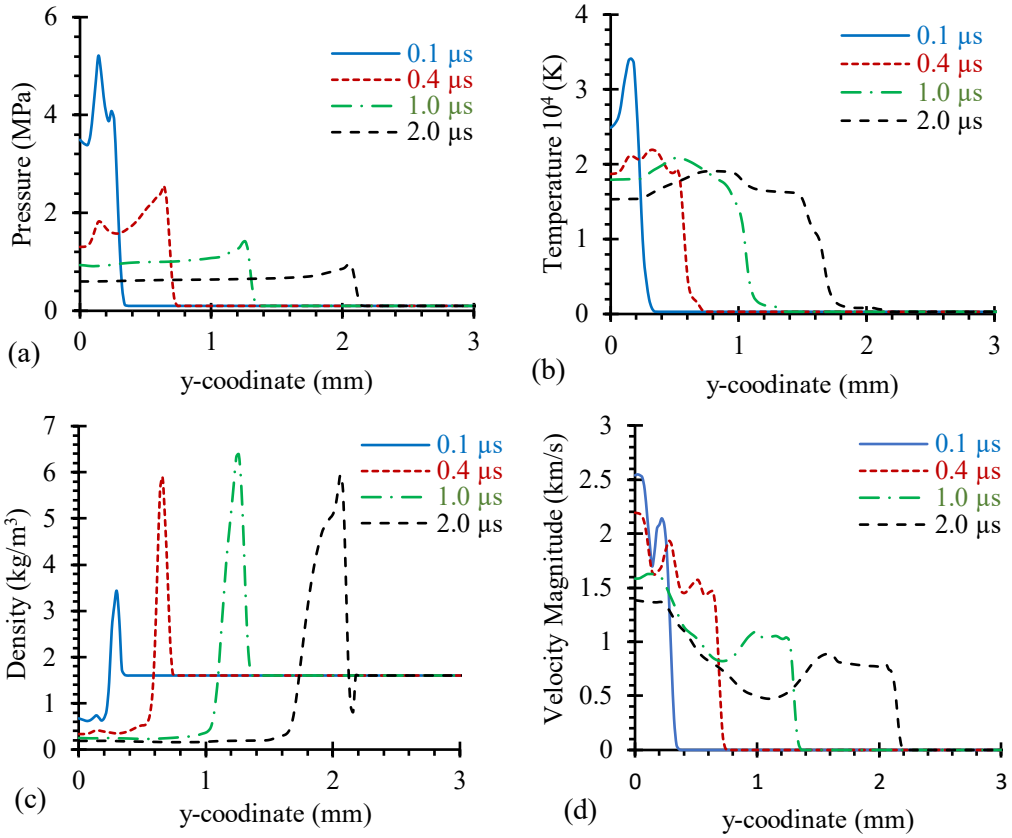

Fig. 11 Profiles of pressure (a), temperature (b), density (c) and velocity (d) along the y-coordinate (symmetry axis) for various times

We have observed that complex interactions may control the development of vortex forms during plume expansion in laser ablation. In the expansion dynamics of laser ablation plasma plumes, mechanisms such as Rayleigh-Taylor Instability (RTI), Richtmyer-Meshkov Instability, Kelvin-Helmholtz Instability, and baroclinic torque (baroclinicity) all play significant roles and sometimes are interconnected with one another (Mahamud et al., 2020; Peng et al., 2023). During laser ablation, plasma plume pushes against the ambient air, and RTI mechanisms develop at the boundaries, creating protrusions which can enhance plume mixing. This mechanism can be triggered by acceleration or deceleration of a density gradient. Shock fronts generated during expansion and plume collisions produce interfacial instabilities, particularly during shock-interface interactions, resulting in impulsive acceleration from laser-driven shock waves. During plume expansion, strong shear develops at the edges of the plume, where high-speed plasma slides past slower-moving ambient gas. This shear leads to vortex roll-up and turbulence. This mechanism can be triggered by velocity gradient across a density boundary. In laser ablation, very strong pressure gradients (from the laser pulse) interact with steep density gradients (e.g., from ambient to plasma), generating localized vorticity and feeding other instabilities. One thing that is true is, these mechanisms are activated during the early expansion of the plumes (Miloshevsky & Hassanein, 2014). The development of RTIs during the early stages of plume expansion is more clearly visible in Fig. 9 and Fig. 10. Additionally, the formation of a Richtmyer-Meshkov instability caused by internal shock propagation is more apparent in Fig. 10 (from 0.1 to 0.4 μs).

4. CONCLUSION

The expansion dynamics of a laser-ablated plasma plume in an air ambience is investigated using transient and compressible flow solvers tPEF, rCF, and sF from OpenFOAM software package. The profiles of pressure, temperature, and mass density along the y-coordinate normal to the surface of target are presented and analyzed. The two-dimensional color maps of pressure and temperature as well as vector fields of velocity evaluated from tPEF, rCF, and sF solvers are reported.

The pressure undergoes a significant abrupt increase at the shock front, followed by the evolution of a rarefaction zone behind it, where, over time, the pressure falls below the surrounding ambient air pressure. At the initial stages, the pressure at the shock front is significantly elevated in the direction that is perpendicular to the surface of the target. Subsequently, the pressure is evenly spread across the whole shock front which could be pointedly relevance in engineering applications involving smooth deposition of multiphase materials. Specific applications are ablating the coating material from a source and letting it deposit onto a surface to be

coated by physical vapor deposition called pulsed laser deposition.

A significant increase in mass density is noted within a narrow layer at the shock front. Following the shock, a wave of reduced mass density, significantly lower than the surrounding air density, emerges within a time frame of mere nanoseconds.

Also, the CFD simulations in quantitative detail accurately replicate the position of the plume. The outcomes of the tPEF solver are evaluated more in detail alongside those from alternative solvers not shown because tPEF comparison is especially intriguing. It uncovers both similarities and differences in the expansion behavior of plasma plumes. The results show how oscillatory regimes of the plume can be significantly relevant to specific engineering applications involving pulsed laser ablation of two or multiphase materials.

The results from two-phase tPEF solver are specifically compared to those produced by single-phase rCF and sF solvers in order to evaluate tPEF's accuracy. Although the data from the solvers have all displayed little differences in their plots and color maps in all cases, these differences are extremely negligible and should have no impact on the tPEF solver's accuracy. The results obtained are similar, so much that tPEF solver can be used as a standard for future work to model multi-species two phase plasma plumes. Also, this study has determined that tPEF solver yields stability and reliability and can be set to have the capacity to simulate plasma plumes when it comes to simulation of multi-species, something rCF and SF solvers cannot be used for. Finally, and this is important for future research, tPEF solver can be used to analyze plasma dynamics and physics processes that take place in multi-phase, multi-species laser-produced plasma plumes.

CONFLICT OF INTEREST

The authors declare no potential conflicts of interest with respect to the research, authorship/contribution, and publication of this original paper.

AUTHORS CONTRIBUTION

Edmund T. Semaha: Developed the study concept, conducted the literature review, gathered and analyzed data, and wrote the manuscript. **Gennady Miloshevsky:** supervised the research, provided critical feedback on the study design and methodology, and helped to revise and refine the manuscript.

REFERENCES

Amidu, M. A., Addad, Y., & Riahi, M. (2020). A hybrid multiphase flow model for the prediction of both low and high void fraction nucleate boiling regimes. *Applied Thermal Engineering*, *178*, 115625. https://doi.org/10.1016/j.applthermaleng.2020.115625

Amoruso, S., Toftmann, B., Schou, J., Velotta, R., & Wang, X. (2004). Diagnostics of laser ablated plasma plumes. *Thin Solid Films*, *453*, 562–572. https://doi.org/10.1016/j.tsf.2003.11.137

Anabitarte, F., Cobo, A., & Lopez-Higuera, J. M. (2012). Laser-induced breakdown spectroscopy: Fundamentals, applications, and challenges. International *Scholarly Research Notices, 2012*. https://doi.org/10.5402/2012/285240

Ayachit, U. (2015). *The paraview guide: A parallel visualization application*. Kitware, Inc. https://dl.acm.org/doi/book/10.5555/2789330

Bai, X., Cao, F., Motto-Ros, V., Ma, Q., Chen, Y., & Yu, J. (2015). Morphology and characteristics of laser-induced aluminum plasma in argon and in air: A comparative study. *Spectrochimica Acta Part B: Atomic Spectroscopy*, *113*, 158–166. http://dx.doi.org/10.1016/j.sab.2015.09.023

Bäuerle, D., & Bäuerle, D. (2011). Surface melting. *Laser Processing and Chemistry*, 177–198. https://doi.org/10.1007/978-3-642-17613-5_10

Cappelli, D. (2018). *A detailed description of reactngTwoPhaseEulerFoam focussing on the links between mass and heat transfer at the phase interface.* Proceedings of CFD with OpenSource Software. Nilsson. H. http://dx.doi.org/10.17196/OS_CFD#YEAR_2018

Chen, G., Xiong, Q., Morris, P. J., Paterson, E. G., Sergeev, A., & Wang, Y. (2014). OpenFOAM for computational fluid dynamics. *Notices of the AMS*, *61*(4), 354–363. http://dx.doi.org/10.1090/noti1095

Chrisey, D. B., & Hubler, G. K. (1994). *Pulsed laser deposition of thin films*.

Chryssolouris, G., Sheng, P., & Choi, W. (1990). Three-dimensional laser machining of composite materials. *Journal of Engineering Materials and Technology,112*(4), 387-392. https://doi.org/10.1115/1.2903347

Dawood, M. S., Hamdan, A., & Margot, J. (2015). Influence of surrounding gas, composition and pressure on plasma plume dynamics of nanosecond pulsed laser-induced aluminum plasmas. *AIP Advances*, *5*(10). https://doi.org/10.1063/1.4935100

Eliceiri, M., & Grigoropoulos, C. P. (2021). Comparison of transient absorption of laser ablation plasma with fundamental plasma absorption relations. *Applied Physics A*, *127*(7), 507. https://doi.org/10.1007/s00339-021-04648-w

Fazio, E., Neri, F., Ponterio, R. C., Trusso, S., Tommasini, M., & Ossi, P. M. (2014). laser controlled synthesis of noble metal nanoparticle arrays for low concentration molecule recognition. *Micromachines*, *5*(4), Article 4. https://doi.org/10.3390/mi5041296

Finko, M. S., & Curreli, D. (2018). Simulation of uranium plasma plume dynamics in atmospheric oxygen produced via femtosecond laser ablation. *Physics of Plasmas*, *25*(8), 083112. https://doi.org/10.1063/1.5034470

Freeman, J., Harilal, S., & Hassanein, A. (2011). Enhancements of extreme ultraviolet emission using prepulsed Sn laser-produced plasmas for advanced lithography applications. *Journal of Applied Physics*, *110*(8). https://doi.org/10.1063/1.3647779

Ghazanfari, V., Salehi, A. A., Keshtkar, A. R., Shadman, M. M., & Askari, M. H. (2019). Numerical simulation using a modified solver within OpenFOAM for compressible viscous flows. *European Journal of Computational Mechanics*, 541–572. https://doi.org/10.13052/ejcm2642-2085.2861

Gómez-Zarzuela, C., Peña-Monferrer, C., Chiva, S., & Miró, R. (2021). Development and validation of a one-dimensional solver in a CFD platform for boiling flows in bubbly regimes. *Progress in Nuclear Energy*, *134*, 103680. https://doi.org/10.1016/j.pnucene.2021.103680

Greenshields, C. J., Weller, H. G., Gasparini, L., & Reese, J. M. (2010). Implementation of semi-discrete, non-staggered central schemes in a colocated, polyhedral, finite volume framework, for high-speed viscous flows. *International Journal for Numerical Methods in Fluids*, *63*(1), 1–21. https://doi.org/10.1002/fld.2069

Gusarov, A. V., & Smurov, I. (2002). Gas-dynamic boundary conditions of evaporation and condensation: Numerical analysis of the Knudsen layer. *Physics of Fluids*, *14*(12), 4242–4255. https://doi.org/10.1063/1.1516211

Gusarov, A. V., Gnedovets, A. G., & Smurov, I. (2000). Gas dynamics of laser ablation: Influence of ambient atmosphere. *Journal of Applied Physics*, *88*(7), 4352–4364. https://doi.org/10.1063/1.1286175

Harilal, S., Miloshevsky, G., Diwakar, P., & LaHaye, N. (2013). Experimental and computational study of complex shockwave dynamics in laser ablation plumes in argon atmosphere. *Physics of Plasmas*, *19*, 083504. https://doi.org/10.1063/1.4745867

Harilal, S., Miloshevsky, G., Diwakar, P., LaHaye, N., & Hassanein, A. (2012). Experimental and computational study of complex shockwave dynamics in laser ablation plumes in argon atmosphere. *Physics of Plasmas*, *19*(8), 083504. https://doi.org/10.1063/1.4745867

Ishii, M., & Mishima, K. (1984). Two-fluid model and hydrodynamic constitutive relations. *Nuclear Engineering and Design*, *82*(2), 107–126. https://doi.org/10.1016/0029-5493(84)90207-3

Issa, R. I. (1986). Solution of the implicitly discretised fluid flow equations by operator-splitting. *Journal of Computational Physics*, *62*(1), 40–65. https://doi.org/10.1016/0021-9991(86)90099-9

Karvatskii, A. Y., Pulinets, I., Lazarev, T., & Pedchenko, A. Y. (2015). Numerical Modellling of Supersonic Flow around a Wedge with the Use of Free Open Software Code OpenFOAM], *Space Science and Technology,* *21*(2), 47–52. https://doi.org/10.15407/knit2015.02.047

Keidar, M., Boyd, I. D., Luke, J., & Phipps, C. (2004). Plasma generation and plume expansion for a transmission-mode microlaser ablation plasma thruster. *Journal of Applied Physics*, *96*(1), 49–56. https://doi.org/10.1063/1.1753658

Kelly, R. (1990). On the dual role of the Knudsen layer and unsteady, adiabatic expansion in pulse sputtering phenomena. *The Journal of Chemical Physics*, *92*(8), 5047–5056. https://doi.org/10.1063/1.458540

Kraposhin, M. V., Ryazanov, D. A., Smirnova, E. V., Elizarova, T. G., & Istomina, M. A. (2017). Development of OpenFOAM solver for compressible viscous flows simulation using quasi-gas dynamic equations. *ISPRAS,* 117–123. https://doi.org/10.1109/ISPRAS.2017.00026

Kraposhin, M., Bovtrikova, A., & Strijhak, S. (2015). Adaptation of kurganov-tadmor numerical scheme for applying in combination with the piso method in numerical simulation of flows in a wide range of mach numbers. *4th International Young Scientist Conference on Computational Science*, *66*, 43–52. https://doi.org/10.1016/j.procs.2015.11.007

Kundrapu, M., & Keidar, M. (2009). Laser ablation of metallic targets with high fluences: Self-consistent approach. *Journal of Applied Physics*, *105*(8), 083302. https://doi.org/10.1063/1.3098198

Kunšek, M., Kljenak, I., & Cizelj, L. (2021). *Comparison of pool scrubbing simulations with POSEIDON-II experiments*. https://www.djs.si/nene2021/proceedings/pdf/NENE2021_410.pdf

Kurganov, A., & Tadmor, E. (2000). New High-Resolution Semi-discrete Central Schemes for Hamilton–Jacobi Equations. *Journal of Computational Physics*, *160*(2), 720–742. https://doi.org/10.1006/jcph.2000.6485

Kuvshinnikov, A. E. & Bondarev, A. E. (2017). *Comparative study of the accuracy for OpenFOAM Solvers.* 2017 Ivannikov ISPRAS Open Conference (ISPRAS), 132–136. https://doi.org/10.1109/ISPRAS.2017.00028

Leboeuf, J., Chen, K. R., Donato, J., Geohegan, D., Liu, C., Puretzky, A., & Wood, R. (1996). Modeling of plume dynamics in laser ablation processes for thin film deposition of materials. *Physics of Plasmas*, *3*(5), 2203–2209. https://doi.org/10.1063/1.871676

Lorenzon, D., & Elaskar, S. A. (2015). *Simulacion de flujos supersonicos bidimensionales y axialmente simetricos con OpenFOAM*.

Mahamud, R., Hartman, D. W., & Tropina, A. A. (2020). Dynamics of dual-pulse laser energy deposition in a supersonic flow. *Journal of Physics D: Applied Physics*, *53*(26), 265201. https://doi.org/10.1088/1361-6463/ab7fd3

Miller, J. C., & Haglund, R. F. (1998). *Laser ablation and desorption* (Vol. 30). Academic Press San Diego.

Miloshevsky, A., Harilal, S. S., Miloshevsky, G., & Hassanein, A. (2014). Dynamics of plasma expansion and shockwave formation in femtosecond laser-ablated aluminum plumes in argon gas at atmospheric pressures. *Physics of Plasmas*, *21*(4). https://doi.org/10.1063/1.4873701

Miloshevsky, G., & Hassanein, A. (2014). Effects of plasma flow velocity on melt-layer splashing and erosion during plasma instabilities. *Nuclear Fusion*, *54*(3), 033008. https://doi.org/10.1088/0029-5515/54/3/033008

OpenCFD Ltd. (2021). http://www.openfoam.com.

OpenFOAM. (2021). http://www.openfoam.com.

Peng, C., Chu, M., Song, Y., Deng, J., & Wu, J. (2023). Study of the effect of magnetic field characteristics on Rayleigh-Taylor instability with density gradient layers. *Computers & Fluids*, *250*, 105726. https://doi.org/10.1016/j.compfluid.2022.105726

Puretzky, A., Geohegan, D., Fan, X., & Pennycook, S. (2000). Dynamics of single-wall carbon nanotube synthesis by laser vaporization. *Applied Physics A*, *70*, 153–160. https://doi.org/10.1007/s003390050027

Rai, V., Yueh, F., & Singh, J. (2007). Laser-induced breakdown spectroscopy of liquid samples. *Laser Induced Breakdown Spectroscopy*, 223–254. https://doi.org/10.1016/B978-044451734-0.50013-2

Saito, K., Sakka, T., & Ogata, Y. H. (2003). Rotational spectra and temperature evaluation of C2 molecules produced by pulsed laser irradiation to a graphite–water interface. *Journal of Applied Physics*, *94*(9), 5530–5536. https://doi.org/10.1063/1.1614431

Shaikh, N. M., Hafeez, S., Rashid, B., & Baig, M. A. (2007). Spectroscopic studies of laser induced aluminum plasma using fundamental, second and third harmonics of a Nd:YAG laser. *The European Physical Journal D*, *44*(2), 371–379. https://doi.org/10.1140/epjd/e2007-00188-3

Singh, R. K., & Narayan, J. (1990). Pulsed-laser evaporation technique for deposition of thin films: Physics and theoretical model. *Physical Review B*, *41*(13), 8843.

Torrisi, L., Gammino, S., Andò, L., & Làska, L. (2002). Tantalum ions produced by 1064 nm pulsed laser irradiation. *Journal of Applied Physics*, *91*(7), 4685–4692. https://doi.org/10.1063/1.1446660

Wang, Q., Jander, P., Fricke-Begemann, C., & Noll, R. (2008). Comparison of 1064 nm and 266 nm excitation of laser-induced plasmas for several types of plastics and one explosive. *Spectrochimica Acta Part B: Atomic Spectroscopy*, *63*(10), 1011–1015. https://doi.org/10.1016/j.sab.2008.06.008

Winefordner, J. D., Gornushkin, I. B., Correll, T., Gibb, E., Smith, B. W., & Omenetto, N. (2004). Comparing several atomic spectrometric methods to the super stars: Special emphasis on laser induced breakdown spectrometry, LIBS, a future super star. *Journal of Analytical Atomic Spectrometry*, *19*(9), 1061–1083. https://doi.org/10.1039/b400355c

Zhigilei, L. V., Lin, Z., & Ivanov, D. S. (2009). Atomistic modeling of short pulse laser ablation of metals: connections between melting, spallation, and phase explosion. *The Journal of Physical Chemistry C*, *113*(27), 11892–11906. https://doi.org/10.1021/jp902294m